However, the partitioning of the waveforms in our data set increases the variance of the observations, currently limiting the ability of this approach to resolve lateral variations in scattering strength.

REFERENCES AND NOTES

1. A. M. Dziewonski and D. L. Anderson, *Phys. Earth Planet. Inter.* **25**, 297 (1981).
2. D. E. Loper and T. Lay, *J. Geophys. Res.* **100**, 6397 (1995).
3. A. Morelli and A. M. Dziewonski, *Nature* **325**, 678 (1987).
4. J. Neuberg and J. Wahr, *Phys. Earth Planet. Inter.* **68**, 132 (1991); A. Rodgers and J. Wahr, *Geophys. J. Int.* **115**, 991 (1993); R. J. Pulliam and P. B. Stark, *J. Geophys. Res.* **98**, 1943 (1993); P. B. Stark and N. W. Hengartner, *ibid.*, p. 1957.
5. W. Menke, *Geophys. Res. Lett.* **13**, 1501 (1986); J. Vidale and H. M. Benz, *Nature* **359**, 627 (1992); K. Bataille and F. Lund, *Geophys. Res. Lett.* **23**, 2413 (1996).
6. D. J. Doornbos, *Phys. Earth Planet. Inter.* **21**, 351 (1980).
7. R. A. Haddon and J. R. Cleary, *ibid.* **8**, 211 (1974); D. J. Doornbos, *Geophys. J. R. Astron. Soc.* **53**, 643 (1978); K. Bataille *et al.*, *Pure Appl. Geophys.* **132**, 151 (1990).
8. K. Bataille and S. M. Flatte, *J. Geophys. Res.* **93**, 15057 (1988).
9. A. C. Chang and J. R. Cleary, *Bull. Seismol. Soc. Am.* **68**, 1059 (1978).
10. Our data, spanning 1988 through 1995, were obtained by means of the IRIS Fast Archive and Recovery Method (FARM). The FARM database contains shallow events (<100 km) with moment magnitude (M_w) ≥5.8 and deep events (>100 km) with M_w ≥5.5.
11. P. S. Earle and P. M. Shearer, *Bull. Seismol. Soc. Am.* **84**, 366 (1994); L. Astiz *et al.*, *Seismol. Res. Lett.* **67**, 8 (1996).
12. Including seismograms with impulsive noise bursts resulting from unrelated earthquakes or instrument error would contaminate the stacked image. Seismograms containing such artifacts were removed by visual inspection. In addition, possible contamination from double events was further avoided by removing traces with impulsive energy arriving before the theoretical *P* arrival. Other seismic phases, including *SS*, *SP*, and *SPP*, overlap a portion of the time-distance window in which the precursors were imaged. However, these phases have a different move-out and are not consistently observed at high frequencies (*11*) because of the high attenuation of the *S* phase.
13. Eighty-nine percent of the CMB is within 10° of a *PKKP* underside CMB reflection point. However, 83% of the reflection points are in the Southern Hemisphere, due to a concentration of seismic stations in the Northern Hemisphere.
14. E. R. Kanasewich, *Time Sequence Analysis in Geophysics* (Univ. of Alberta Press, Alberta, Canada, 1981).
15. We subtracted the average noise from a 60-s window starting 140 s before the *PKKPbc* arrival. Shifting the noise window to a time that overlaps with the precursory wave train changes the precursors' zero offset but not their shape.
16. The maximum amplitude was taken from the processed trace in a 15-s window starting at the theoretical *PKKPbc* arrival time.
17. The weight assigned to a processed trace was defined as the ratio of the maximum value found in a signal window to that taken in a noise window. An incorrect choice for the position of the noise window can bias the amplitude of the precursors, highlighting the importance of the *P*-wave test (Fig. 2C). A gap between the end of the noise window and the start of the reference phase will falsely amplify the observed precursors by ~5%. This was verified in stacks using *P* as a reference phase. A false precursory wave train was imaged, for distance ranges with poor STN, when using a noise window ending 50 s before the *P* arrival time. A noise window that overlaps the precursory time window may reduce the amplitude of the observed precursors, down-weighting seismograms with large-amplitude precursors. This effect is negligible, given that the amplitude of the noise on a single trace is up to 10 times greater than that of the precursors. Thus, we use a 140-s noise window ending 5 s before *PKKPbc* and a 15-s signal window starting at the *PKKPbc* onset time. It is also possible for the stack to be biased by an anomalously large reference phase (possibly resulting from focusing effects); this was avoided by assigning a maximum weight of 7 to each individual trace. Although the choice of noise window and weighting scheme can influence the absolute level of the observed precursors, the relative amplitude of the *PKKPbc* precursors with range was independent of the choice of windowing.
18. The source-receiver range for deep events was corrected to its zero depth equivalent by ray tracing from the hypocenter to the surface with the use of the *PKKPbc* ray parameter.
19. B. Efron and R. Tibshirani, *Science* **253**, 390 (1991).
20. I. Tolstoy and C. S. Clay, *Ocean Acoustics: Theory and Experiment in Underwater Sound* (McGraw-Hill, New York, 1966); P. Scott and D. Helmberger, *Geophys. J. R. Astron. Soc.* **72**, 237 (1983); J. A. Ogilvy, *Theory of Wave Scattering from Random Rough Surfaces* (Institute of Physics, London, 1991).
21. W. Kampfmann and G. Müller, *Geophys. Res. Lett.* **16**, 653 (1989).
22. The extreme values for the grid search were $\lambda = 5$ to 30 km and $\sigma = 100$ to 1000 m. In general, increasing σ scaled the amplitude of the predicted precursory and increasing λ concentrated the energy near the *PKKPbc* arrival.
23. A model of CMB topography could not be found that fit our observations within their error bounds over the entire distance range, giving rise to the possibility of additional sources of scattering. Thus, limits were placed on the model parameters by consideration of models that matched the general character of the observations. Synthetics for $\lambda < 7$ km predict a precursory wave train that does not monotonically increase with time at shorter distance ranges, which is a result of the increased contribution of *ab*-to-*ab* scattering. Synthetics calculated for $\lambda > 10$ m concentrate the observed energy near the *PKKPbc* arrival.
24. G. Poupinet *et al.*, *Nature* **305**, 204 (1983); A. Morelli *et al.*, *Geophys. Res. Lett.* **13**, 1545 (1986); J. H. Woodhouse *et al.*, *ibid.*, p. 1549; P. M. Shearer and K. M. Toy, *J. Geophys. Res.* **96**, 2233 (1991); K. C. Creager, *Nature* **356**, 309 (1992); P. M. Shearer, *J. Geophys. Res.* **99**, 19647 (1994); W. J. Su and A. M. Dziewonski, *ibid.* **100**, 9831 (1995); X.-D. Song and D. V. Helmberger, *ibid.*, p. 9805.
25. E. R. Engdahl, thesis, Saint Louis University, St. Louis, MO (1968).
26. R. A. W. Haddon, *Eos* **53**, 600 (1972); M. Hedlin *et al.*, *Nature* **387**, 145 (1997).
27. E. R. Engdahl, *Science* **161**, 263 (1968).
28. P. G. Richards, *Geophys. J. R. Astron. Soc.* **35**, 243 (1973).

29. We thank the personnel from the IRIS-GSN stations for providing the data and specifically R. Benson for maintaining the FARM archive. This work benefited from the suggestions of B. Engdahl, two anonymous reviewers, and many co-workers and was supported by NSF grant EAR93-15060.

4 March 1997; accepted 5 June 1997

Seismic Evidence of Partial Melt Within a Possibly Ubiquitous Low-Velocity Layer at the Base of the Mantle

J. Revenaugh* and R. Meyer

Three source regions show evidence of a low-velocity layer that is less than 15 kilometers thick on top of the core-mantle boundary and require about a 3:1 ratio of shear-to-compressional velocity reduction, which is consistent with partial melt. Layer thickness is correlated with travel time residuals of the seismic phases that are most sensitive to the lowermost mantle velocity. These observations suggest that the layer is thinned beneath downwellings but is present everywhere along the core-mantle boundary. Low viscosity accompanying partial melt can localize the upwelling of warmed mantle, making the low-velocity layer a plausible source of mantle plumes.

Recent seismic work has mapped several anomalously slow regions of the lowermost mantle, taking the form of an ultra–low-velocity layer ≤40 km thick on top of the core-mantle boundary (CMB) (*1*, *2*). *P* wave velocity (ν_P) within the layer is as much as 10% lower than that of the overlying mantle. Partial melt offers an explanation of the layer (*3*) and predicts a 30% shear wave velocity (ν_S) drop within the layer (*3*, *4*). Because the CMB approximates an isotherm, this hypothesis also predicts layer ubiquity in the absence of substantial compositional heterogeneity. We tested these predictions by searching for reflections from the layer in seismograms recorded by California regional arrays.

PcP, the high-frequency compressional-wave reflection from the CMB, is often used to study the detailed structure of the boundary (*5*). Its typically low signal-to-noise ratio necessitates the use of array data to avoid misinterpretation of noise as an anomalous structure. Precursors to *PcP* due to reflection or scattering from lowermost mantle structures are further buried in noise (*2*, *6*). To detect them and measure their amplitude

J. Revenaugh, Institute of Tectonics, University of California, Santa Cruz, CA 95064, USA.
R. Meyer, Department of Geological Sciences, University of California, Santa Barbara, CA 93106, USA.

*To whom correspondence should be addressed.

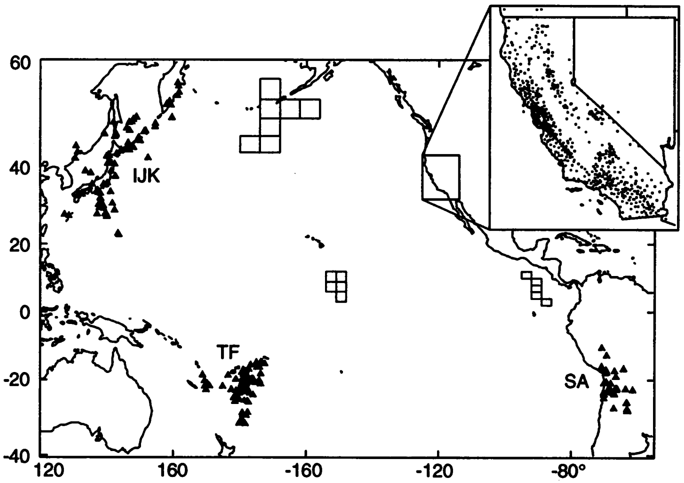

Fig. 1. Mercator projection showing the earthquakes (triangles), stations of the California regional seismic networks (inset; dots), and outlines of bins used to stack the CMB bouncing *PcP* phases, each containing an average of 512 bounce points.

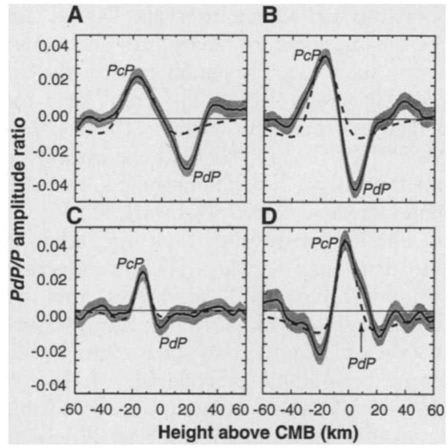

Fig. 2. (**A**) Stack of 5509 seismograms for events in the TF subduction complex for target reflectors in the lowermost mantle (solid line). Only a single midpoint bin was used, which ignored structural variation near the bounce points of *PdP*. Gray shading denotes 95% confidence intervals of the data stack as determined by the bootstrap method. Synthetic stack (dashed line) contains only *PcP* arrivals. (**B**) As in (A), except that data were separately stacked in five 3° by 3° bounce point bins and aligned before final stacking. (**C**) Binned stack of 2892 seismograms of events in the IJK subduction complex. (**D**) Binned stack of 1607 seismograms of events in SA. Note the normal-polarity, closely spaced precursor to *PcP* (arrow).

and phase, we used a stacking algorithm that, unlike traditional and double-beam forming (*7*), presupposes a target phase. Here that phase is *PdP*, a *PcP*-like reflection from a lower mantle discontinuity.

Defining τ_{ij}^{P} as the travel time of *P* for the *i*th event recorded by the *j*th station and $\tau_{ij}^{PdP}(d)$ as the arrival time of *PdP* reflected from a discontinuity at depth *d* (*8*), we obtained the stack from

$$R(d) = \sum_i \sum_j S_{ij}\,[\tau_0 + \tau_{ij}^{PdP}(d) - \tau_{ij}^{P}] \qquad (1)$$

where the seismograms $S_{ij}(t)$ (where *t* is time) are aligned with *P* at time τ_0 and *R* is the mean reflector strength (*9*). When the source and receiver arrays are small and the paths of *P* and *PdP* are similar, the amount of stack degradation due to travel time heterogeneity is small. As used here, both arrays are large, and the paths of *P* and *PdP* diverge by as much as 1000 km. To reduce the effect of incoherence on the stack, we summed wave forms in small *PdP* bounce-point bins that measure 2° to 6° on a side (Fig. 1). Once obtained, these bin stacks were aligned on peak amplitude and summed to produce a final composite stack. Alignment on peak amplitude is justified by the consistency of stack shape and the small dispersion of peak amplitude depths (<20 km, equivalent to travel time shifts of <1 s). Bins with fewer than 150 hits or poorly defined peaks were not summed. Modeling with randomly time-shifted synthetic data suggests no more than ±0.6 s of remaining travel time variability.

For the Tonga-Fiji (TF) subduction complex, a peak above the 95% confidence level in the lowermost mantle was identified as *PcP*, and a precursory shallower trough was identified as a reverse-polarity reflection (the sign opposite of *P* and *PcP*) from a discontinuity about 14 km above the CMB (Fig. 2A). A precursor is needed to explain the stack because, although the stacked synthetic *PcP* wave form is slightly asymmetric (*10*), the magnitude of the shallow trough is much less than observed and it is not possible for us to mimic the trough simply by summing variably delayed *PcP* phases. This is consistent with a previous study of this region that modeled wave forms for two nearly co-located events included in our data set (*2*). The primary difference between our results and those of (*2*) is in the peak stack amplitude, which is only 2.5% of *P* in this study. We take this as evidence of stack degradation due to travel time heterogeneity.

Peak *PcP* amplitude depths range from 27 to 11 km below the CMB in the five bin stacks for events in TF (Fig. 1), signifying a delayed *PcP* arrival and lower-than-average velocities in D″, the lowermost 200 to 300 km of the mantle (Fig. 2B). Peak aligned stack amplitude is increased over that of the nonbin stack, and there is noticeable compaction of the stack peaks, which indicates reduction in travel time variability due to binning.

To estimate the mean depth, reflection coefficient, and remaining travel-time variability of *PcP* and the precursory *PdP* phase, 20,000 Monte Carlo synthetic data sets were generated, stacked, and compared with the observed stack. For *PcP* and *PdP*, there exist trade-offs between *R* and the travel-time variability (σ) (*11*). There is also a trade-off between *R* and the thickness of the layer [the low-velocity layer (LVL)] separating the CMB from the *PdP* reflector (H_{LVL}) because *PcP* and *PdP* are separated in time by less than the dominant period (~1 s). Models were accepted if they accounted for greater than 80% of stack variance, a value chosen with reference to the

Table 1. Means, standard deviations, and ranges of the adjustable parameters for the acceptable model subset.

Source region	Events (*n*)	Records (*n*)	*PcP*			*PdP*			H_{LVL} (km)
			d (km)	*R*	σ (s)	*d* (km)	*R*	σ (s)	
TF	111	4217	2895 ± 7	0.01 to 0.13 0.05 ± 0.03	0.3 ± 0.1	2880 ± 5	−0.14 to 0.00 −0.05 ± 0.03	0.3 ± 0.1	14 ± 5
IJK	83	2892	2893 ± 9	0.00 to 0.13 0.02 ± 0.02	0.2 ± 0.1	2881 ± 7	−0.12 to 0.00 −0.02 ± 0.02	0.3 ± 0.1	11 ± 6
SA	52	1607	2887 ± 6	0.00 to 0.11 0.04 ± 0.02	0.2 ± 0.1	2880 ± 8	−0.03 to 0.12 0.02 ± 0.03	0.3 ± 0.1	8 ± 3

bootstrap confidence intervals. Table 1 lists the means, standard deviations, and ranges of the six adjustable parameters for the acceptable model subset. The basal layer has velocities possibly much lower than IASP91 (8), so H_{LVL} could be in error by as much as 10 to 30%. Nonetheless, our estimate agrees with previous work (2).

The composite bin stack for events in the Izu-Japan-Kurile (IJK) subduction complex (Fig. 2C) resembles the TF source region stack, although the IJK stack is somewhat more compact because of different ray-parameter coverage. A Monte Carlo exploration of model space (Table 1) results in a mean layer thickness of 11 ± 5 km for IJK. Although the range of acceptable models is large, it also appears that the precursory reflection is weaker in this stack. The stack of South American (SA) events (Fig. 2D) shows that the precursory phase is not reversed and arrives close to *PcP*. These observations are borne out by the Monte Carlo simulations, which have a mean layer thickness of 8 ± 3 km and *PdP* reflection coefficients ranging from −0.03 to 0.12 with a mean value of 0.02 (Table 1).

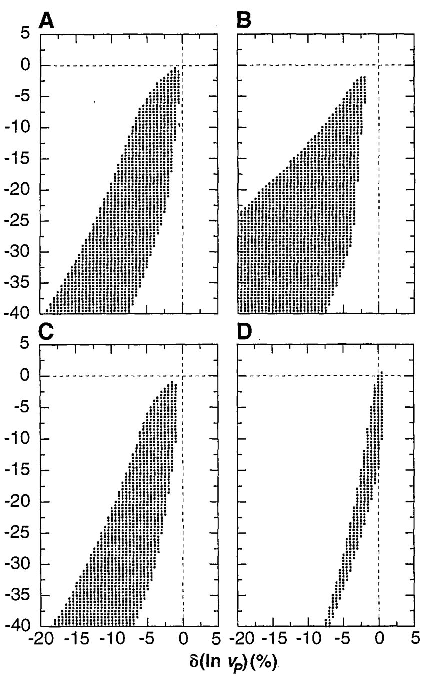

Fig. 3. (**A**) Dots indicate acceptable velocity variations across a first-order discontinuity that is assumed to be responsible for the *PdP* precursor to *PcP* for events in TF. Negative values signify a velocity decrease across the discontinuity. (**B**) As in (A), except that the discontinuity is modeled as a 5-km-wide transition zone. (**C**) As in (A) for events in the IJK subduction complex. (**D**) As in (A) for events in SA.

For the TF and IJK stacks (Fig. 2, B and C), all acceptable models have reversed-polarity *PdP*. The amplitude of *PdP* relative to *P* can be used to estimate the velocity and density contrasts of the reflector. A grid search was conducted over v_S, v_P, and density perturbations, in which a mean reflection coefficient was computed for each perturbation triplet (12). Triplets predicting *R* to within a factor of 2 of the observed range of *PdP* reflection strengths were accepted (13). Both v_S and v_P must drop across the layer to produce the observed reversed polarity reflections (Fig. 3, A and C). Furthermore, a nearly 3:1 ratio of v_S to v_P decrease is needed. Density was allowed to vary between −3% and 10% and was found to have little effect on the sign or magnitude of computed reflection coefficients. We also addressed the effects of a 5-km-wide *PdP* transition for the TF source region (14). The effect of a broadened transition is to increase the minimum acceptable velocity perturbations and the range of acceptable v_S to v_P ratios (Fig. 3B).

It would appear that the stack for SA (Fig. 2D) is fundamentally different from TF and IJK. Reflection coefficient modeling, however, belies this initial impression (Fig. 3D). Although the precursory arrival in the SA stack apparently has normal polarity, an LVL atop the CMB is still favored (15). Broadening the width of the *PdP* transition to 5 km further extends the range of acceptable solutions to small positive v_S and v_P perturbations, such that we cannot rule out a slightly faster (≤2.5%) than normal layer on top of the CMB, but the results are still consistent with an LVL for SA.

Analysis of *PcP* precursor amplitudes requires about a 3:1 ratio of v_S to v_P decrease in a thin layer on top of the CMB. Our modeling approach does not constrain the absolute drops, but work with core-diffracted phases in other areas (1) requires as large as 10% v_P drops within the LVL. Extrapolating those results to this study suggests v_S drops of 30 to 50%. These numbers are consistent with the presence of partial melt (3, 4). Whether similar ratios can be achieved solely by compositional variation, such as iron enrichment in a basal mixing layer (3, 16), is uncertain.

An inverse relation exists between H_{LVL} and long-wavelength diffracted *P* velocity ($v_{P_{diff}}$) (17) in D″ (Fig. 4A). The layer is thicker in regions of low $v_{P_{diff}}$, consistent with depressed v_P within it. We observed a similar correlation between $v_{P_{diff}}$ and *PcP* travel-time delays ($\delta\tau_{PcP}$) (Fig. 4B). The magnitudes of the inferred $\delta\tau_{PcP}$ are larger by a factor of 2 than those that would be produced by a thin (≤15 km) layer with a 10% v_P decrease, which implies a correlation between the D″ velocity structure and a basal layer thickness in which the layer is thickened under upwellings (TF) and thinned under downwellings (SA) but is potentially ubiquitous.

Although the large errors preclude any sort of quantitative analysis, we note that the estimates of range-adjusted mean *PdP* reflection coefficients decrease as the layer thins, implying diminished velocity drops within the basal layer. If melt rains down from the overlying mantle (18), a thick, melt-rich, and seismically very slow layer would accumulate beneath hot D″ and mantle upwelling, whereas a thin melt-poor layer would accumulate beneath downwellings. This does not, however, account for the sharp upper boundary of the LVL (2). An alternative is iron enrichment within the LVL. Chemical reactions between silicate liquids and iron readily occur (19). An LVL partially isolated from general mantle circulation by negatively buoyant melt and low viscosity (20) could become iron enriched, increasing density and further decreasing seismic velocities (3). Lateral flow within the LVL could collect iron-rich material beneath upwellings, relating layer thickness to velocity drop.

Models of deep-mantle plume formation emphasize the role of a thin low-viscosity channel (21). With increasing thermal age, the channel thickens, becomes dynamically unstable, and eventually erupts hot material. We suggest that the partially molten LVL, with its attendant low viscosity, is this channel and is thus a source of mantle plumes.

Fig. 4. (**A**) Comparison of the mean P_{diff} velocity perturbation and thickness of the LVL (H_{LVL}). (**B**) Comparison of the mean P_{diff} velocity perturbation (2) and *PcP* residual relative to IASP91 at vertical incidence ($\delta\tau_{PcP}$). Although the latter is subject to large uncertainty, the sense of the delay is consistent with known D″ heterogeneity.

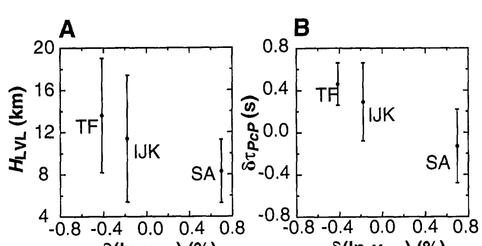

REFERENCES AND NOTES

1. E. Garnero and D. V. Helmberger, *Phys. Earth Planet. Inter.* **91**, 161 (1995); *Geophys. Res. Lett.* **23**, 977 (1996); E. Garnero, S. Grand, D. V. Helmberger, *ibid.* **20**, 1843 (1993).
2. J. Mori and D. V. Helmberger, *J. Geophys. Res.* **100**, 20359 (1995).
3. Q. Williams and E. J. Garnero, *Science* **273**, 1528 (1996).

4. J. P. Watt, G. F. Davies, R. J. O'Connell, *Rev. Geophys. Space Phys.* **14**, 541 (1976); R. J. O'Connell and B. Budiansky, *J. Geophys. Res.* **82**, 5719 (1977).
5. H. Kanamori, *J. Geophys. Res.* **72**, 559 (1967); J. Schlittenhardt, *J. Geophys.* **60**, 1 (1986); J. E. Vidale and H. M. Benz, *Nature* **359**, 627 (1993).
6. F. Krüger, M. Weber, F. Scherbaum, J. Schlittenhardt, *Geophys. Res. Lett.* **20**, 1475 (1993); *Geophys. J. Int.* **122**, 637 (1995); F. Krüger, F. Scherbaum, M. Weber, J. Schlittenhardt, *Bull. Seismol. Soc. Am.* **86**, 737 (1996); F. Scherbaum, F. Krüger, M. Weber, *J. Geophys. Res.* **102**, 507 (1997).
7. Traditional stacking assumes that travel-time variation across the array is a linear function of the great-circle distance from the source. This is valid for small aperture arrays and teleseismic data but limits stacking to a single source or sources that are essentially co-located. Double-beam stacking (*6*) relaxes the latter restriction, stacking over receiver and source arrays and resulting in improved slowness and azimuth resolution. The source array aperture, however, must be small in comparison with epicentral distance. With an assumption of a target phase, we can use our approach to stack over large arrays.
8. B. L. N. Kennett, in *International Association of Seismology and Physics of the Earth's Interior (IASPEI) 1991 Seismological Tables*, B. L. N. Kennett, Ed. (Research School of Earth Sciences, Australian National University, Canberra, Australia, 1991), pp. 164–167. We modified the model by depressing the CMB 100 km while retaining the lowermost mantle velocity gradients. This allowed us to compute *PcP* and *PdP* times appropriate for a slow D″ velocity layer without having to alter the overlying velocity structure (for example, slow *PcP* would map as a reflector below the nominal CMB). Ellipticity corrections were applied to the predicted *P* and *PdP* times, the latter approximated by the tabulated correction for *PcP*. Because our focus was on the lowermost mantle, the error in this approximation was ≤0.01 s.
9. Stacking was preceded by alignment of *P* wave forms and deconvolution of the source-time function. Alignment of *P* reduced travel-time variability due to shallow velocity structure and source mislocation. Aligned wave forms were averaged to eliminate variable station-side contributions, leaving the source-time function convolved against a mean mantle response. This was deconvolved from the aligned wave forms, reducing interevent variation of wave form shape to <10% of peak amplitude.
10. To obtain the synthetic stack, we generated ray-theory synthetic data matching the distance distribution of the source region data set and consisting of *P* and *PcP*, the only phases occurring in the absence of a lower mantle reflector. The synthetic seismograms were convolved with the mean deconvolved *P* wave form (*9*) before they were stacked.
11. Residual travel-time variability is parameterized as the standard deviation of a zero-mean Gaussian perturbation applied to delay time in the synthetics.
12. Velocities above the reflector were fixed at IASP91 values for the mean discontinuity depth. We obtained the mean plane-layer reflection coefficient by averaging over the ray parameter weighted by the ray-parameter distribution of stacked data.
13. Amplitudes of *PdP* are affected by variations in lowermost mantle attenuation, velocity heterogeneity, and reflector topography. The factor of 2 expansion of the acceptable range of *R* is intended to avoid the introduction of biases from these factors and from approximations inherent to ray theory. We also required that the resulting mean *PcP* reflection coefficient be positive and less than 0.42 (0.33 for SA) after we applied the same perturbations to velocity and density at the CMB. This constraint eliminates models with large compressional to shear velocity variation ratios. The maximum value for each source region is a factor of 3 greater than the largest accepted estimate (Table 1) to allow for unmodeled variations in geometric spreading and possibly severe attenuation within the LVL.
14. Velocity and density vary linearly across the transition. To compute the mean reflection coefficient, we took the magnitude of the complex reflection coefficient at peak frequency and ignored wave form distortion effects.
15. ν_S and ν_P increases produce *PdP* and *PcP* reflection coefficients that are too large. Some Monte Carlo models had reversed-polarity *PdP*. Eliminating these and accepting only those triplets that predict normal-polarity *PdP* do not affect our conclusions.
16. E. Knittle and R. Jeanloz, *Science* **251**, 1438 (1991); F. Goarant, F. Guyot, J. Peyronneau, J.-P. Poirier, *J. Geophys. Res.* **97**, 4477 (1992); R. Jeanloz, in *Relating Geophysical Structures and Processes: The Jeffreys Volume*, K. Aki and R. Dmowska, Eds., vol. 76 of *Geophysical Monograph Series* (American Geophysical Union, Washington, DC, 1993), pp. 121–127.
17. M. E. Wysession, *Nature* **382**, 244 (1996).
18. S. M. Rigden, T. J. Ahrens, E. M. Stolper, *Science* **226**, 1071 (1984).
19. E. Ito, K. Morooka, O. Ujike, T. Katsura, *J. Geophys. Res.* **100**, 5901 (1995).
20. N. H. Sleep, *Geophys. J. R. Astron. Soc.* **95**, 437 (1988).
21. F. D. Stacey and D. E. Loper, *Phys. Earth Planet. Inter.* **33**, 45 (1983); N. H. Sleep, *J. Geophys. Res.* **97**, 20007 (1992).
22. This research was supported by NSF and Lawrence Livermore National Laboratory, Institute of Geophysics and Planetary Physics. This is Institute of Tectonics contribution 308.

3 March 1997; accepted 17 June 1997

Distance-Dependent Electron Transfer in DNA Hairpins

Frederick D. Lewis,* Taifeng Wu, Yifan Zhang, Robert L. Letsinger, Scott R. Greenfield, Michael R. Wasielewski

The distance dependence of photoinduced electron transfer in duplex DNA was determined for a family of synthetic DNA hairpins in which a stilbene dicarboxamide forms a bridge connecting two oligonucleotide arms. Investigation of the fluorescence and transient absorption spectra of these hairpins established that no photoinduced electron transfer occurs for a hairpin that has six deoxyadenosine-deoxythymidine base pairs. However, the introduction of a single deoxyguanosine-deoxycytidine base pair resulted in distance-dependent fluorescence quenching and the formation of the stilbene anion radical. Kinetic analysis suggests that duplex DNA is somewhat more effective than proteins as a medium for electron transfer but that it does not function as a molecular wire.

The occurrence of long-range electron transfer (ET) in duplex DNA remains controversial (*1*). Does the π system of stacked base pairs in B-form DNA function as a molecular wire or as an insulator? Barton and co-workers (*2–5*) have reported several lines of evidence in support of efficient long-range ET involving an electronically excited intercalated metal complex and either a second intercalated metal complex or a "natural" electron donor such as guanine or thymine dimer. The observation of efficient fluorescence quenching in systems with randomly intercalated metal complexes (*2*) and a synthetic 15–base pair duplex in which a donor complex was tethered to the 5′ end of one oligomer and an acceptor complex was tethered to the 5′ end of its complement (*3*) was attributed to the occurrence of long-range ET. This interpretation has recently been questioned on both experimental (*6–8*) and theoretical (*9*) grounds. Current commentaries on this controversy have pointed out the need to determine systematically the dependence of the ET rate constant on the distance separating the donor and acceptor in a series of structurally well-defined supramolecular systems in which the ET process can be directly monitored (*1*).

We report here the results of our investigation of the distance dependence of the photoinduced ET in a family of synthetic DNA hairpins in which a stilbenedicarboxamide forms a bridge connecting two oligonucleotide arms. One of our laboratories previously described the synthesis of thermodynamically stable stilbene-containing hairpins with stems consisting of three or more dA-dT or dG-dC base pairs (*10*). Hairpins with dA-dT stems are fluorescent, whereas hairpins with dG-dC stems are nonfluorescent. Photoinduced ET from guanine to the stilbene singlet state provides a plausible but untested mechanism for fluorescence quenching. Because the transient absorption spectra of both the stilbene singlet state (*11*) and its anion radical

F. D. Lewis, T. Wu, Y. Zhang, R. L. Letsinger, Department of Chemistry, Northwestern University, Evanston, IL 60208, USA.
S. R. Greenfield, Chemistry Division, Argonne National Laboratory, Argonne, IL 60439, USA.
M. R. Wasielewski, Department of Chemistry, Northwestern University, Evanston, IL 60208, and Chemistry Division, Argonne National Laboratory, Argonne, IL 60439, USA.

*To whom correspondence should be addressed. E-mail: lewis@chem.nwu.edu